

1 Introduction

The Sun, our star, is a powerful source of non-thermal radio emission. Solar radio bursts provide insight into the Sun’s magnetic field, coronal processes, and the solar wind. A wide range of spacecraft and ground-based instruments monitor the Sun at radio wavelengths as well across the electromagnetic spectrum in order to understand heliophysical processes. These observatories also contribute to forecasting potentially dangerous space weather that can wreak havoc on navigation, communications, and power grids. This paper describes HeRO (**H**eliophysics **R**adio **O**bserver), a hybrid ground and space instrument to map and track type II and III solar radio bursts as they propagate from the solar corona out into the interplanetary medium. HeRO will be capable of tracking type II and III radio bursts with unprecedented spatial resolution through the use of multi-baseline radio interferometry from 300 MHz to 100 kHz. This paper describes HeRO’s science goals (Section 2), mission design (Section 3), and expected performance (Section 4). The advantages of a vector sensor antenna for the space portion of HeRO is discussed in Section 3.3.

2 HeRO Science

2.1 Science Objectives

The solar corona, the solar wind, and the interplanetary medium are natural laboratories for fundamental plasma physics. HeRO will take advantage of these natural laboratories to address three science objectives:

1. Determine the location, shape, and properties of coronal and interplanetary shocks
2. Determine the site and conditions for efficient particle acceleration
3. Trace open magnetic fields along which energetic particles propagate

These three objectives can be addressed by remote observation of type II and III radio bursts across frequency (and corresponding solar distance) with high temporal and spatial resolution. Figure 1 shows that HeRO (composed of ground-based HeRO-G and space-based HeRO-S) will track solar radio bursts from the corona ($1.03 R_{Sun}$) to 0.5 AU ($90 R_{Sun}$).

2.2 Type II and III Radio Bursts

When the shock wave from a coronal mass ejection (CME) accelerates already-energized electrons present in the ambient plasma, the resulting type II emission reflects the morphology and motion of both the shock front and the CME, as well as the geometry of the local magnetic field. These type II bursts occur a few times per month, radiating both at the fundamental and the second harmonic of the local plasma frequency. As the

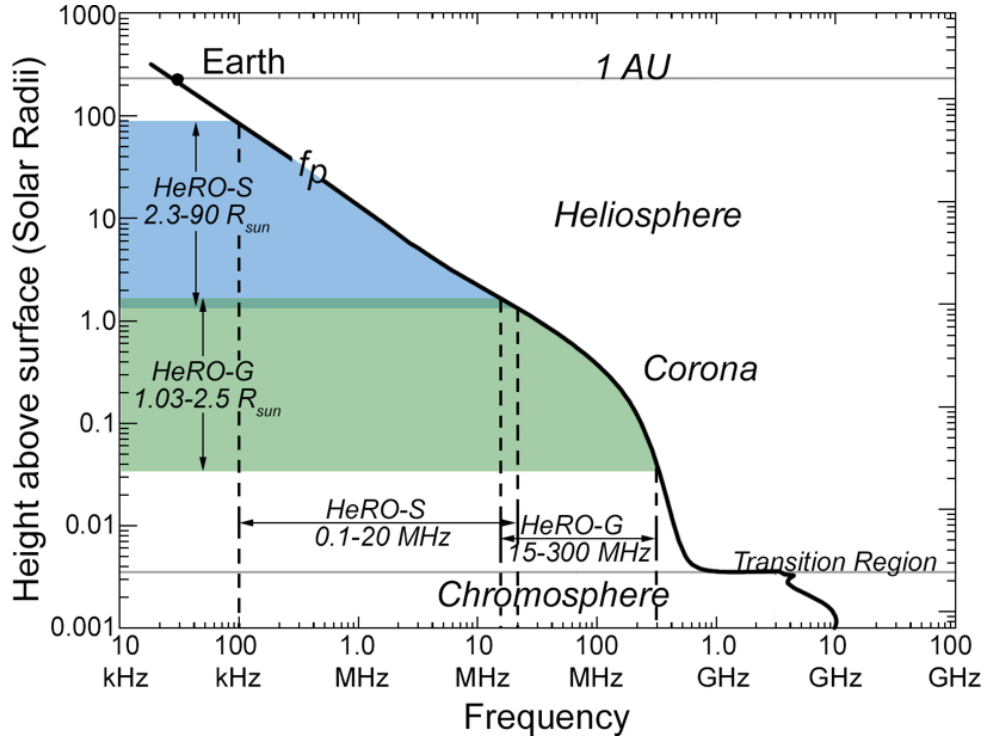


Figure 1: Plasma frequency as a function of solar distance. The green shaded portion of the plot shows HeRO-G coverage. The blue shaded area shows HeRO-S coverage. HeRO (HeRO-S + HeRO-G) covers 100 kHz – 300 MHz in frequency and 1.03 – 90 R_{Sun} .

56 disturbance propagates outward into lower density plasma the emission drifts from higher
 57 to lower frequency, with typical timescales of minutes to hours. Note that some diffuse
 58 type II-like bursts may be due to gyrosynchrotron emission, rather than plasma emission,
 59 although this remains speculative [Bastian, 2007; Pohjolainen et al., 2013].

60 Type III bursts are brief, lasting seconds to minutes, but are much more common than
 61 type IIs. Magnetic reconnection events accelerate energetic electrons across a broad range
 62 of heliocentric distances, resulting in fast-moving ‘beams’ of electrons propagating along
 63 magnetic field lines at appreciable fractions of the speed of light. These beams radiate at
 64 the fundamental and second harmonic with a broad distribution of starting frequencies,
 65 drifting rapidly to lower frequencies.

66 The burst phenomena to be studied by HeRO are initiated close to the solar surface
 67 and propagate far out into interplanetary space. We are interested in tracking both type
 68 II-producing shock waves and type III-producing electron beams along this full range of
 69 distances, for different reasons. For type II bursts, we follow the evolution of the radio-
 70 emitting regions (objective 1), due to electron acceleration and which are presumably the
 71 sites of ion acceleration as well, to better understand how the shock parameters (speed,
 72 Mach number, magnetic field geometry) affect the conditions of efficient acceleration
 73 (objective 2). We are interested in the entire lifecycle of the shock, in particular the
 74 ‘hot spots’ of particle acceleration at its front or flank, from the time the radio emission
 75 first develops in the low corona, transits the mainly-closed-field regions below the ‘source
 76 surface’ [Culhane et al., 2014], enters the solar-wind-dominated region, and then sweeps

77 through ever larger portions of the heliosphere.

78 For type III bursts, we are mainly interested in defining the radio-emitting electron beam
79 trajectories throughout their lifetimes. By remotely measuring the precise emission lo-
80 cation as the type III burst propagates outward, the magnetic field line along which the
81 electron beam is propagating can be mapped. A full understanding of these events, and
82 the answers to the science questions posed, demands observations spanning the full range
83 of frequency from event initiation to the limits imposed by the plasma frequency at the
84 HeRO-S orbit. In practice, this means from a few hundred MHz to 100 kHz. Conse-
85 quently, HeRO is designed to operate across this full range simultaneously, with no gaps,
86 from 100 kHz to 300 MHz. Because the radio emission is due to plasma emission, there
87 is a one-to-one correspondence between emitting frequency and distance from the Sun,
88 shown graphically in Figure 1.

89 **2.3 Spot Mapping**

90 Using radio interferometry techniques, HeRO measures the location of type II and type III
91 burst emissions with 20 to 2000 times better accuracy than current space-based instru-
92 ments, depending on frequency, and with both improved precision and wider frequency
93 coverage than current ground-based instruments. This supports the production of de-
94 tailed spot maps comprising collections of precise centroid locations vs. frequency and
95 time. Such spot maps have been shown (e.g. in Chen et al. [2015]) to delineate complex,
96 fine-scale spatial structure well below the apparent size of individual sources. This capa-
97 bility is new, unique and scientifically powerful in the context of the science objectives
98 posed in Section 2.1.

99 Spot maps are frequency- and time-dependent centroid positions valid when the source
100 morphology is dominated by a single, point-like source. This is expected to be the case
101 with solar radio bursts as long as the time-frequency cells are small. Accordingly, both
102 HeRO-S and HeRO-G arrays are designed such that they span comparable physical extents
103 of 10 km, corresponding to an accuracy of interferometric phase calibration requirement
104 of 2° and an interferometric signal-to-noise ratio (SNR) of 30. Precise relative calibration
105 benefits from the ability to form closure quantities, requiring a minimum of 3 antennas
106 for phase and 4 for amplitude. The HeRO-S design with 6 antennas provides 10 phase
107 and 9 amplitude closure quantities, and adequate constraints for detecting and modeling
108 simple non-point-like sources in addition to measuring centroid positions. HeRO thereby
109 maintains the required angular precision across the entire 100 kHz to 300 MHz range. To
110 support the scientific goals, HeRO-S and HeRO-G must present a 2D array configuration
111 projected into the solar direction at all times. Furthermore where the structure being
112 observed has an angular extent comparable to or larger than the interferometer fringe
113 spacing, a range of baseline orientations and lengths permits source size to be estimated.
114 HeRO-G stations are designed with true imaging capability, while the 6 HeRO-S spacecraft
115 provide 15 baselines for this purpose.

3 HeRO Design

HeRO is a hybrid instrument composed of a ground-based component for frequencies above the ionospheric cut-off (15–300 MHz) and a space-based component covering lower frequencies not accessible from the ground (100 kHz–20 MHz). Both components operate simultaneously to form a single instrument with frequency coverage from 100 kHz–300 MHz. Both HeRO-S and HeRO-G will make use of the spot mapping technique described in Section 2.3. HeRO could have been implemented entirely on a space-based platform, but data storage and clock stability requirements for the higher end of the HeRO frequency band would have made the spacecraft unnecessarily complicated and costly. Instead, the requirements for HeRO-S were simplified by setting the frequency upper limit at 20 MHz (maintaining overlap with HeRO-G). Position knowledge, sampling rate, and data rate requirements are significantly relaxed at 20 MHz vs. 300 MHz, reducing the cost and complexity of HeRO-S.

Both HeRO-S and HeRO-G will record raw voltage data to their respective ring buffers. When an event is identified, either by autonomous triggering (HeRO-G) or by ground-in-the-loop examination of dynamic spectra (HeRO-S), the portion of the buffer containing the event will be frozen and flagged for download or collection. The buffer size on both HeRO segments is sufficiently large for multiple events to be saved while continuing to use the remaining memory in ring buffer mode. HeRO-G events will be used to flag relevant data in the HeRO-S ring buffer and vice versa.

3.1 HeRO-S

HeRO-S(pace) comprises a flock of 6 identical 6U (30 x 20 x 10 cm) CubeSats, each with antenna, receiver, position and timing synchronization, precision clock, and memory management. For interferometry of solar radio bursts, the 6 spacecraft are positioned such that the baselines range from 0.5-10 km, in an optimized 3-D arrangement. For transient objects such as solar radio bursts, traditional aperture synthesis based on evolving baseline projections is not possible, but ‘snap-shot’ interferometry nevertheless allows precision metrology of centroids for single, compact sources, from which spot maps can be generated as a function of time and frequency.

HeRO-S uses a vector sensor as its antenna. The directivity of the Lincoln Laboratory Vector Sensor (VS) (Section 3.3) provides the capability to determine the direction of arrival and the polarization sense of incoming waves, allowing spatial and polarization steering of the antenna beam or nulling of interference sources. This allows HeRO-S to adaptively suppress noise from Earth-derived sources by an estimated 30 dB compared to conventional methods, such that solar radio bursts will dominate the result [Knapp et al., 2016a]. Without such nulling capabilities, avoidance of strong terrestrial emissions of both natural and artificial origin would require deployment to a distant location such as a Lagrange point or lunar orbit, severely constraining downlink rates. Positioning HeRO-S above the plasmapause minimizes plasmaspheric masking and distortion over the entire 0.1-20 MHz frequency range while remaining close enough to the Earth for efficient high data rate communication.

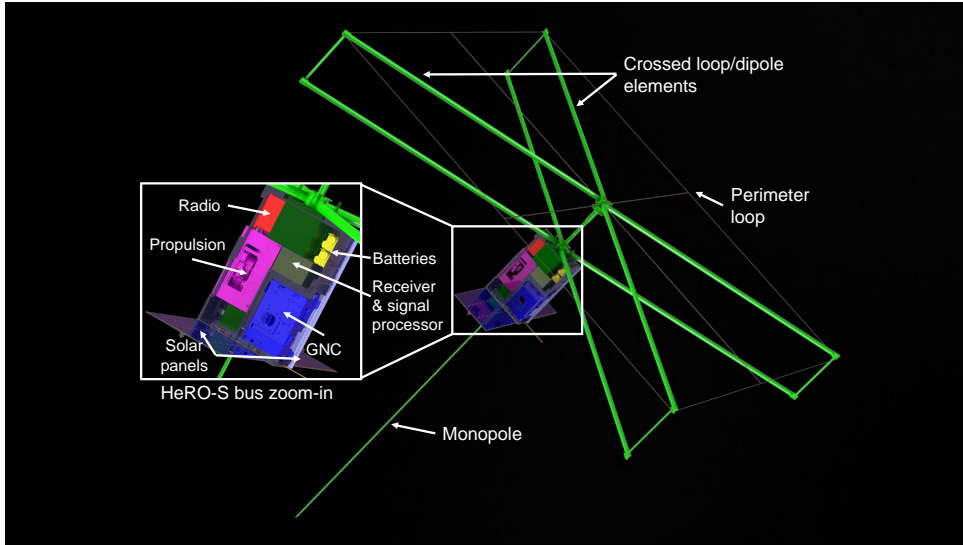


Figure 2: The 6U HeRO-S spacecraft. The vector sensor is composed of two crossed loop/dipole arms, a perimeter loop around the tips of the loop/dipoles, and a monopole. False colors are used to highlight key subsystems.

157 HeRO-S CubeSats will fly in loose formation in an elliptical, slightly skewed geosyn-
 158 chronous (S-GEO) orbit. The S-GEO orbit provides the benefits of a GEO orbit while
 159 never transiting the crowded GEO belt. Requirements for stationkeeping of the space-
 160 craft are not stringent. Knowledge of relative spacecraft position is sufficient to establish
 161 array coherence, and can be refined to high accuracy by the interferometry itself. Position
 162 knowledge to 1/10–1/16 of a wavelength is generally considered sufficient for interfero-
 163 metric baselines, so HeRO-S’s position knowledge requirement is 1.5-1 m at 20 MHz —
 164 well within the capability of standard ranging systems. Each spacecraft carries a chip-
 165 scale atomic clock for precision timing. Each HeRO-S spacecraft will have a small electric
 166 propulsion system for initial orbit adjustment, stationkeeping, reaction wheel desatura-
 167 tion, and disposal at end of life. The stationkeeping requirements for the S-GEO orbit
 168 are minimal (~ 64 m/s ΔV).

169 HeRO-S will observe the sun for 16 hours per day and store raw voltages in a ring buffer
 170 which can hold up to 32 hours of data. During the remaining 8 hours, when the Earth
 171 and plasmasphere are between the HeRO-S flock and the Sun, HeRO-S will downlink
 172 data that has been flagged as containing an event based on ground-in-the-loop exami-
 173 nation of summary dynamic spectra from each node. HeRO-S will take advantage of a
 174 large dedicated X-band ground station to downlink decimated raw data for correlation on
 175 the ground rather than attempting to cross-correlate in space and downlink the visibili-
 176 ties. Retaining the raw data enables iterative tuning and adjustment of the correlation
 177 process for a particular observation, and allows iterative estimation of instrumental cali-
 178 bration parameters. In this respect, the data from both HeRO-S and HeRO-G will allow
 179 more processing flexibility than the visibility-only data that is produced by most major
 180 observatories.

181 HeRO-S will be calibrated using a stable NIST-traceable noise diode or comb generator,
 182 depending on the specific calibration. The calibration signal will be injected into the

183 six antenna inputs [Dicke, 1946; Meloling et al., 2015] to determine channel-to-channel
184 gain and phase differences as well as the absolute gain of the receiver system. The VS
185 antenna element gains as a function of angle are measured by rotation of the spacecraft
186 while observing a known reference such as a ground-based source. Traditional radio in-
187 terferometry techniques like self-calibration will be used in post-processing on the ground
188 after correlation. To suppress self-electromagnetic interference (EMI), all HeRO subsys-
189 tems are selected for low noise and are shielded. Several spacecraft subsystems, including
190 propulsion and communication, are turned off during data acquisition. The EMI spec-
191 trum is evaluated throughout development and the affected frequency ranges affected are
192 constrained where EMI cannot be eliminated entirely.

193 3.2 HeRO-G

194 HeRO-G is the ground-based component of HeRO (15–300 MHz). HeRO-G is composed
195 of two geographically separated ‘stations’, each of which contains 25 HeRO-G nodes with
196 UV coverage optimized for solar observing (Figure 3b). Together, the two HeRO-G sta-
197 tions will provide 16+ hours of solar observation per day. The HeRO-G nodes are based
198 on the RAPID (**R**adio **A**rray of **P**ortable **I**nterferometric **D**etectors) node design [Lind
199 et al., 2013, 2015]. RAPID is currently under development at MIT Haystack Observatory
200 in collaboration with Cambridge University. Each RAPID node is physically indepen-
201 dent, equipped with a high performance direct digitization receiver, hot-swappable solid
202 state disk (SSD) storage, precision clock, solar and battery power, and optional wireless
203 interconnection.

204 Each HeRO-G node will use a variant of the SKALA antenna [de Lera Acedo et al., 2015]
205 for 50–300 MHz (Figure 3a) and a simplified LWA antenna [Ellingson, 2011] for 15–50
206 MHz. Both antennas will operate simultaneously using a common base. Raw voltage
207 signals from HeRO-G antennas are captured, filtered, decimated, compressed, and time-
208 tagged before being transferred to the solid state drive (SSD) ring buffer in the HeRO-G
209 base unit.

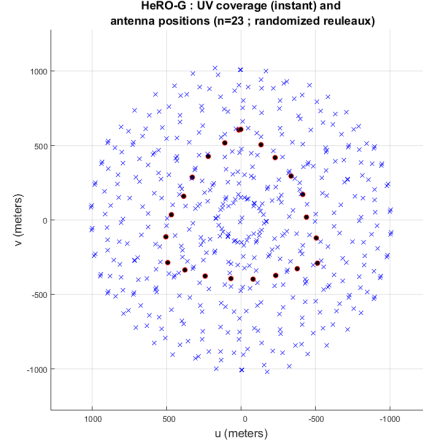
210 Three connected inner HeRO-G nodes in a vector sensing configuration serve as a trigger-
211 ing system that semi-autonomously identifies solar bursts from their compact, transient,
212 and spectrally narrow features and their angular location relative to the solar position. A
213 successful detection causes raw data to be retained locally and a trigger to be sent to the
214 outlying, unconnected nodes via Iridium or other satellite provider. The trigger informs
215 the other nodes to mark this data for retention and notifies the operator of automati-
216 cally detected events. Data are collected manually by swapping the solid state disks and
217 transferring them to a centralized cloud computing facility. This is performed no less fre-
218 quently than once per month, or when the buffer fills to a threshold capacity. Triggering
219 thresholds will be set so that the buffer does not overflow too quickly.

220 3.3 Vector Sensor

221 A vector sensor is composed of three loops and three dipoles with a common phase cen-
222 ter that capture the three components of the magnetic field in addition to the electric



(a) HeRO-G field unit with SKALA antenna.



(b) Antenna positions and instantaneous (u,v) coverage for HeRO-G station

Figure 3: HeRO-G field unit (a) and HeRO-G station layout (b). There are 25 HeRO-G units per station, arranged in a randomized Reuleaux triangle (red dots) to achieve uniform (u,v) plane filling (blue x). Baseline lengths range from 100 m – 10 km.

223 field 3-vector [Nehorai and Paldi, 1994]. The six elements of the vector sensor allow a
 224 complete characterization of incident electromagnetic fields, including full polarization
 225 measurement. In the HeRO-S deployable vector sensor, two crossed elements simultane-
 226 ously provide loop and dipole modes [King, 1959; Robey et al., 2016]. A perimeter loop
 227 provides the third loop antenna along with mechanical stability, and a monopole provides
 228 the sixth element. The HeRO-S vector sensor, shown in green in Figure 2, is stowed in
 229 a 1U volume (10x10x10 cm) and deployed in two stages. The loop/dipoles are 4 m long,
 230 the monopole is 2 m long, the horizontal loop area is 8 m² and the two vertical loops are
 231 each 1 m² [Robey et al., 2016]. Further discussion on vector sensors for astronomical ap-
 232 plications can be found in Knapp et al. [2016a], Robey et al. [2016], Knapp et al. [2016b],
 233 and Volz et al. [2016].

234 4 HeRO Performance

235 4.1 Sensitivity

236 Figure 4 compares HeRO sensitivity with type II and III burst intensities. Even for
 237 a single-baseline, HeRO-S and HeRO-G have sufficient SNR to detect and characterize
 238 nearly all expected type II and III bursts over their entire frequency range. More baselines
 239 will further improve performance. HeRO’s instrumental noise floor is set by the galactic

240 sky noise except at the lowest frequencies. Comparing HeRO’s sensitivity or system-
 241 equivalent flux density (SEFD, solid black curve in Figure 4) to an average spectrum of a
 242 type III burst (dotted red curve), a signal-to-noise ratio (SNR) of at least 30 is maintained
 243 across all frequencies.

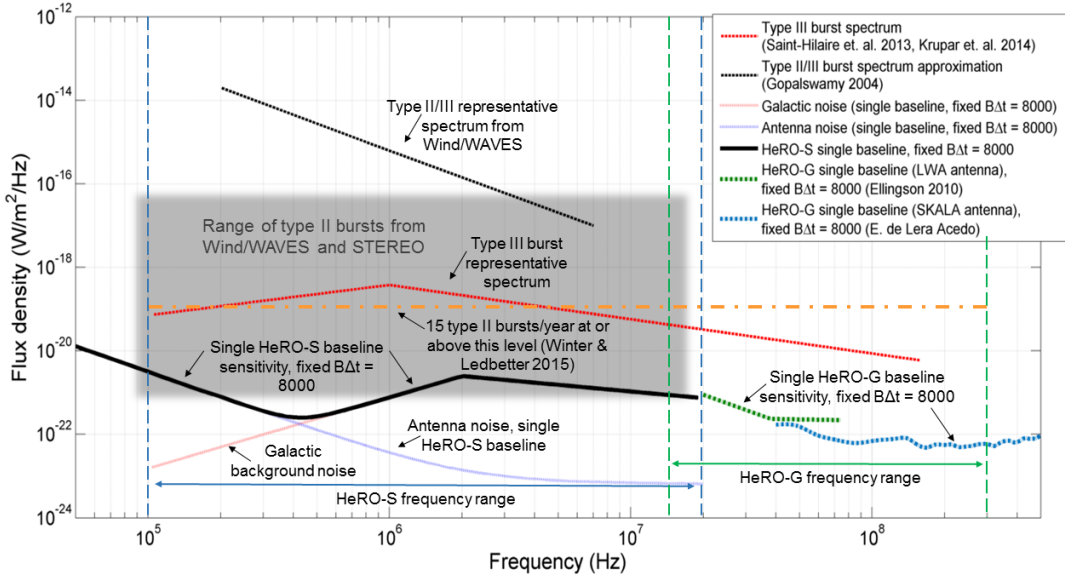


Figure 4: HeRO Sensitivity compared with expected solar radio burst flux. A single baseline of HeRO-S or HeRO-G will detect type II and III solar bursts over several decades of intensity and frequency. Shown for comparison are an average type III burst spectrum, scaled to an occurrence rate of 3 bursts per day (red); the range of type II bursts recorded by Wind/WAVES and STEREO over several years (gray box); the intensity of both type II and type II bursts observed by Wind/WAVES (black dashed); HeRO-S SEFD (solid black), the quadrature sum of antenna noise (purple) and galactic background (red) assuming a time-bandwidth product $B\Delta t = 8000$; HeRO-G SEFD for LWA antenna (green) and SKALA antenna (cyan). HeRO-G sees substantially less galactic noise than HeRO-S because of the limited field of view.

244 Not shown in Figure 4 but of significance is Auroral Kilometric Radiation (AKR), which is
 245 due to the electron cyclotron maser instability above the Earth’s auroral ring. Generally
 246 occurring below 500 kHz, AKR is narrowly beamed into frequency-dependent hollow cones
 247 aligned with the magnetic field direction in the source region [Mutel et al., 2008; Menietti
 248 et al., 2011], is highly variable, and exhibits modulation with dayside emissions being
 249 weaker and less frequent. Time occupancies at the peak frequency of ~ 300 kHz are in the
 250 20–40% range [Panchenko et al., 2009]. Fortunately, AKR is strongly beamed away from
 251 the equator, is weaker and less frequent during the dayside HeRO-S observations, and is
 252 weakest during solar maximum. Any radiation reaching HeRO-S at $6R_{Earth}$ will appear
 253 compact, on the order of 1° , and can be nulled by the VS.

254 4.2 Angular Resolution

255 HeRO’s astrometric precision is defined in terms of a ‘spot’, i.e. a datum with position,
 256 flux, polarization, time and frequency values at a specific location in this 6D space. Spot
 257 position accuracy for a single baseline in one dimension is determined by the fringe spacing
 258 θ

$$\theta = \frac{\lambda}{B} = \frac{103 \text{ arcmin}}{\nu_{MHz}}, \quad B_{max} = 10 \text{ km} \quad (1)$$

259 multiplied by the phase error expressed as a fraction of 2π . This is given by $(2\pi \cdot \text{SNR})^{-1}$,
 260 which will vary depending on the radio flux density. For the specified SNR of 30 corre-
 261 sponding to a phase error of 2° , the spot location precision will be

$$\theta = \frac{\lambda}{B \cdot 2\pi \text{SNR}} = \frac{0.6 \text{ arcmin}}{\nu_{MHz}} \quad (2)$$

262 This corresponds to 0.03 arcmin at 20 MHz and 6 arcmin at 100 kHz. These accura-
 263 cies refer to relative measurements between observations nearby in time and frequency,
 264 delineating scientifically meaningful structures in the sources. Modeling indicates that
 265 6 CubeSats (15 baselines) meet requirements for all expected sources, while as few as
 266 4 (6 baselines) can locate features with degraded accuracy. HeRO’s angular resolution
 267 performance is summarized in Figure 5.

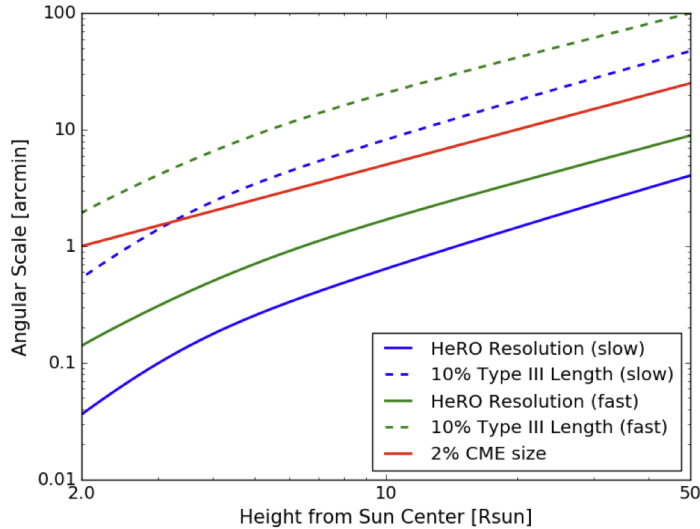


Figure 5: For type II bursts, HeRO-S requires centroid position accuracy $<2\%$ of the CME size (red line) [Gopalswamy and N., 2010]. For type III, HeRO requires 10% of the length of the electron beam based on a burst duration measurement [Alvarez and Haddock, 1973]. Green and blue dashed and solid lines compare modeled accuracy for slow and fast bursts [You et al., 2007].

268 5 Conclusions

269 HeRO, alone and in concert with existing and planned observatories, will significantly
 270 enhance our understanding of the solar corona, the dynamic interplanetary medium and

271 magnetic field, and particle acceleration processes. In addition to performing ground-
272 breaking heliophysics on its own, HeRO will directly support the in situ measurements
273 of Solar Probe Plus (SPP) and Solar Orbiter (SO) during their cruise phases and close
274 approaches to the Sun.

275 If HeRO were to launch in early 2022 near the next predicted solar maximum, HeRO
276 expects to witness 20-40 radio-loud CMEs [Winter and Ledbetter, 2015] and to capture $2/3$
277 of them in its one-year life — a sufficient sample to reveal the underlying physics. Type
278 III radio bursts occur much more frequently, providing a sample of many hundreds to
279 thousands of type III events. HeRO will track type II and III bursts with unprecedented
280 angular and spectral resolution over half of the Earth-Sun distance. HeRO represents
281 a major improvement in angular resolution capability, particularly at low frequencies
282 (HeRO-S). As such, there is strong potential that HeRO will observe previously unknown
283 phenomena in addition to addressing its primary science objectives.

284 Acknowledgements

285 The authors thank the extended HeRO team: Ryan Volz, Geoff Crew, Phil Erickson, Alan
286 Fenn, Alex Morris, Mark Silver, Kerry Johnson, Divya Oberoi, Juha Vierinen, Angelos
287 Vourlidis, Stephen White, Kamen Kozarev, Sarah Klein, Sara Seager, Fash Azad, Will
288 Rogers, Tom Brown.

289 Generous support for the development of the vector sensor for astrophysical applications
290 provided by the Lincoln Laboratory Advanced Concepts Committee.

291 References

- 292 Alvarez, H. and F. T. Haddock. Decay time of type III solar bursts observed at kilometric
293 wavelengths. *Solar Physics*, **30**, 1, 175–182, 1973.
- 294 Bastian, T. S. Synchrotron Radio Emission from a Fast Halo Coronal Mass Ejection. *The*
295 *Astrophysical Journal*, **665**, 1, 805–812, 2007.
- 296 Chen, B., T. S. Bastian, C. Shen, D. E. Gary, S. Krucker, and L. Glesener. Particle
297 acceleration by a solar flare termination shock. *Science*, **350**, 6265, 2015.
- 298 Culhane, J. L., D. H. Brooks, L. van Driel-Gesztelyi, P. Démoulin, D. Baker, M. L.
299 DeRosa, C. H. Mandrini, L. Zhao, and T. H. Zurbuchen. Tracking Solar Active Region
300 Outflow Plasma from Its Source to the Near-Earth Environment. *Solar Physics*, **289**,
301 10, 3799–3816, 2014.
- 302 de Lera Acedo, E., N. Razavi-Ghods, N. Troop, N. Drought, and A. J. Faulkner. SKALA,
303 a log-periodic array antenna for the SKA-low instrument: design, simulations, tests
304 and system considerations. *Experimental Astronomy*, 2015.
- 305 Dicke, R. H. The Measurement of Thermal Radiation at Microwave Frequencies. *Review*
306 *of Scientific Instruments*, **17**, 7, 268, 1946.

- 307 Ellingson, S. W. Sensitivity of Antenna Arrays for Long-Wavelength Radio Astronomy.
308 *IEEE Transactions on Antennas and Propagation*, **59**, 6, 1855–1863, 2011.
- 309 Gopalswamy, N. and N. Corona Mass Ejections: a Summary of Recent Results. *Pro-*
310 *ceedings of the 20th National Solar Physics Meeting, held 31 May - 4 June, 2010 in*
311 *Papradno, Slovakia, p. 108-130*, pp. 108–130, 2010.
- 312 King, R. The rectangular loop antenna as a dipole. *IRE Transactions on Antennas and*
313 *Propagation*, **7**, 1, 53–61, 1959.
- 314 Knapp, M., F. Robey, R. Volz, F. Lind, A. Fenn, A. Morris, M. Silver, S. Klein, and
315 S. Seager. Vector antenna and maximum likelihood imaging for radio astronomy. In
316 *IEEE Aerospace Conference Proceedings*, vol. 2016-June, 2016a.
- 317 Knapp, M., R. Volz, F. Lind, F. Robey, A. Fenn, K. Johnson, M. Silver, A. Morris, and
318 S. Klein. HF vector sensor for radio astronomy: Ground testing results. In *AIAA Space*
319 *and Astronautics Forum and Exposition, SPACE 2016*, 2016b.
- 320 Lind, F. D., C. J. Lonsdale, A. J. Faulkner, P. Alexander, and C. Mattmann. Radio array
321 of portable interferometric detectors (RAPID). In *2013 IEEE International Symposium*
322 *on Phased Array Systems and Technology*, pp. 676–683. IEEE, 2013.
- 323 Lind, F. D., C. J. Lonsdale, A. J. Faulkner, C. Mattmann, N. Razavi-Ghods,
324 E. de Lera Acedo, P. Alexander, J. Marchese, R. McWhirter, C. Eckert, J. Vierin-
325 en, R. Schaefer, W. Rideout, R. Cappallo, V. Pankratius, D. Oberoi, S. Khudikyan,
326 M. Joyce, C. Goodale, M. Boustani, L. Cinquini, R. Verma, and M. Starch. Radio
327 Array of Portable Interferometric Detectors (RAPID): Development of a deployable
328 multiple application radio array. In *2015 International Conference on Electromagnetics*
329 *in Advanced Applications (ICEAA)*, pp. 1337–1340. IEEE, 2015.
- 330 Meloling, J., J. W. Rockway, M. P. Daly, A. R. Monges, J. C. Allen, W. R. Nielsen,
331 P. M. McGinnis, R. B. Thompson, and N. A. Mozaffar. An Advanced HF Direction
332 Finding Vector-Sensing Antenna System. Tech. Rep. January, SPAWAR System Center
333 Technical Report 2069, 2015.
- 334 Menietti, J. D., R. L. Mutel, I. W. Christopher, K. A. Hutchinson, and J. B. Sigwarth.
335 Simultaneous radio and optical observations of auroral structures: Implications for
336 AKR beaming. *Journal of Geophysical Research: Space Physics*, **116**, A12, n/a–n/a,
337 2011.
- 338 Mutel, R. L., I. W. Christopher, and J. S. Pickett. Cluster multispacecraft determination
339 of AKR angular beaming. *Geophysical Research Letters*, **35**, 7, n/a–n/a, 2008.
- 340 Nehorai, A. and E. Paldi. Vector-sensor array processing for electromagnetic source lo-
341 calization. *IEEE Transactions on Signal Processing*, **42**, 2, 376–398, 1994.
- 342 Panchenko, M., M. L. Khodachenko, A. G. Kislyakov, H. O. Rucker, J. Hanasz, M. L.
343 Kaiser, S. D. Bale, L. Lamy, B. Cecconi, P. Zarka, and K. Goetz. Daily variations of
344 auroral kilometric radiation observed by STEREO. *Geophysical Research Letters*, **36**,
345 6, L06102, 2009.

- 346 Pohjolainen, S., H. Allawi, and E. Valtonen. Origin of wide-band IP type II bursts.
347 *Astronomy & Astrophysics*, **558**, A7, 2013.
- 348 Robey, F., M. Knapp, A. Fenn, M. Silver, K. Johnson, F. Lind, R. Volz, S. Seager, and
349 F. Neylon-Azad. High Frequency (HF) Radio Astronomy from a Small Satellite. In
350 *30th Annual AIAA/USU Conference on Small Satellites*, 2016.
- 351 Volz, R., M. Knapp, F. Lind, and F. Robey. Covariance Estimation in Terms of Stokes
352 Parameters with Application to Vector Sensor Imaging. In *50th Asilomar Conference*
353 *on Signals, Systems and Computers*. Pacific Grove, CA, 2016.
- 354 Winter, L. M. and K. Ledbetter. Type II and Type III Radio Bursts and Their Correlation
355 With Solar Energetic Proton Events. *The Astrophysical Journal*, **809**, 1, 105, 2015.
- 356 You, X. P., G. B. Hobbs, W. A. Coles, R. N. Manchester, and J. L. Han. An Improved
357 Solar Wind Electron Density Model for Pulsar Timing. *The Astrophysical Journal*,
358 **671**, 1, 907–911, 2007.